International Journal of Heat and Technology
Vol. 44, No. 4, August, 2026, pp. 1588-1598
Journal homepage: http://iieta.org/journals/ijht

Experimental and Numerical Investigation of the Effects of Obstacle Geometry on Mixed-Convection Heat Transfer and Thermo-Hydraulic Performance in a Vertical Air Channel

Sajjad Isam Mohammed*, Hussein Mahmood Jassim

College of Engineering, Department of Mechanical Engineering, University of Babylon, Hilla 51001, Iraq

Corresponding Author Email: sajaad.mohamed1230@student.uobabylon.edu.iq

Copyright: ©2026 The authors. This article is published by IIETA and is licensed under the CC BY 4.0 license (http://creativecommons.org/licenses/by/4.0/).

https://doi.org/10.18280/ijht.440422

Received: 8 June 2026
Revised: 14 August 2026
Accepted: 24 August 2026
Available online: 31 August 2026

Keywords:
mixed convection, vertical air channel, heat transfer enhancement, Nusselt number, obstacle geometry, thermo-hydraulic performance

ABSTRACT

This study experimentally and numerically compared four obstacle geometries in a vertical air channel to examine the influence of geometry on mixed-convection heat transfer and pressure drop. To vary blockage, curvature, edge sharpness, and characteristic length while maintaining similar exposed heat-transfer area, a rectangle, a circular cylinder, an equilateral triangle, and a square were chosen. In contrast to prior studies investigating isolated configurations, all geometries were assessed at the same nominal operating conditions. Tests were conducted at total heating powers of 200 and 300 W and inlet velocities of 2–6 m s^{-1}, yielding 40 cases. A three-dimensional COMSOL model using the shear-stress transport (SST) k–ω turbulence model and the Boussinesq approximation was validated against the measurements, with differences in the average Nusselt number (*Nu*) ranging from 10% to 15%. As the Reynolds number (*Re*) increased, the heat transfer coefficient (HTC) increased, whereas the surface temperature and the Richardson number (*Ri*) decreased. The circular cylinder produced the highest HTC. The rectangle yielded the highest average *Nu* and relative performance evaluation criterion (PEC) of approximately 1.40 with a relatively low pressure drop. The triangle caused the highest pressure drop, and the square was used as a PEC reference. Under the studied conditions, the rectangle exhibited the best thermo-hydraulic performance.

1. INTRODUCTION

Mixed convection in a vertical air channel results from the interaction between forced airflow and buoyancy and plays an important role in the design of compact heat exchangers, electronic cooling passages, and thermal management systems. In these applications, heated internal obstacles can model heat-producing components, heat-sink inserts, or passive flow-control elements placed in confined cooling compartments. These obstacles increase convective heat removal by disrupting the thermal boundary layer and causing the flow to separate, recirculate, and mix. However, the resulting blockage also leads to higher pressure loss and increased fan power needed to maintain airflow. Thus, obstacle selection is a thermo-hydraulic design problem that involves the trade-off between heat-transfer enhancement and hydraulic penalty [1, 2].

In numerical investigations of mixed convection in vertical channels and buoyancy-assisted flow in rectangular ducts, the influence of the Richardson number (*Ri*) on wall heat transfer was found to be substantial. *Ri* quantifies the balance between forced airflow and buoyancy, and an almost periodic reversal of flow was reported under some operating conditions [3, 4].

Experimental investigations of mixed convection showed that the averaged Nusselt number (*Nu*) and pressure drop increased with the Reynolds number (*Re*), also dependent on duct inclination in the case of mixed convection in a rectangular air duct supplied with a centered heated plate [5]. A CFD study confirmed that fin geometry and geometric parameters had an impact on *Nu*, *f*, and pressure drop [6]. However, these studies considered a single heated plate or plate-fin configuration and did not compare different heated obstacle geometries under identical vertical mixed-convection conditions.

Three-dimensional simulations of a heated T-shaped fin in a ventilated enclosure indicated that the flow structure and average *Nu* were strongly affected by *Re* and *Ri*, although only one fin geometry was studied and no associated pressure-loss penalty was assessed [7]. Systematic numerical investigations of three square cylinders controlled by a partition and oblique inverted L-shaped obstacles showed that the arrangement and inclination of these obstacles significantly altered flow separation, recirculation, and mixing in fluids that compress convective heat transfer. Nevertheless, both studies examined only particular obstacle configurations and did not provide direct comparisons of different heated obstacle cross-sections under identical conditions [8, 9].

A numerical study investigated a rectangular air duct fitted with polygonal and trapezoidal ribs and reported that the highest *Nu* and thermo-hydraulic performance were achieved using polygonal shapes. In another numerical investigation on a three-dimensional rectangular air channel, it was found that square baffles and triangular obstacles have profound effects on wake development, fluid mixing, and *Nu* [10, 11].

Numerical investigations showed that cylinder blockage and position, as well as baffle–obstacle arrangement, strongly

affected wake development, fluid mixing, and heat transfer. However, these studies were restricted to specific configurations and did not compare various heated obstacle geometries under similar vertical mixed-convection conditions [12, 13]. Three-dimensional mixed-convection simulations around slanted pin fins in a vertical air channel demonstrated that fin inclination, bypass ratio, and *Ri* all had significant effects on flow redistribution and average *Nu*. However, a single pin-fin cross-section was used in this study, and thus the influence of heated obstacle shape on thermo-hydraulic performance could not be directly assessed [14].

A numerical investigation into airflow characteristics of a channel with separated obstacles revealed that obstacle orientation and configuration controlled flow separation, recirculation, thermal-boundary-layer distortion, and pressure loss. However, it considered only two-dimensional forced convection instead of three-dimensional mixed convection in a vertical channel that has a different shape and dimension of the heated obstacle [15]. Numerical investigations of flexible baffles and a confined circular cylinder in air channels showed that geometric blockage altered fluid mixing, wall temperature, and flow resistance. Flexible baffles reduced the pressure drop by 16.5% with a *Nu* increase of only 3.4%. Lastly, the blockage ratio minimizing wall temperature differed from that maximizing mass flow in the naturally convecting channel. Yet, these studies never compared together heated shapes of obstacles at the same vertical mixed convection conditions [16, 17]. Experiments and three-dimensional simulations showed that truncated-rib design and fin-channel length profoundly influenced heat transfer and thermo-hydraulic performance. Optimized straight ribs increased global thermo-hydraulic performance by up to 12.16%, while predictions for rectangular fins agreed with measurements within 4.28%; along the way, they identified that shorter developing channels provided greater heat transfer than longer ones. Both studies considered forced convection and specific rectangular features rather than contrasting different heated shapes under vertical mixed-convection conditions [18, 19]. Advanced heat transfer performance of baffled channels: A review was performed that verified the effect of baffle shape, blockage ratio, and Reynolds number (*Re*) on the trade-off between heat-transfer improvement and friction losses in directionally baffled channels, whereas mixed-convection articles remain limited compared with forced-convection studies. Hence, it emphasized the need to conduct detailed experiments supported by numerical simulations to identify configurations that offer enhanced heat transfer with minimal flow-energy requirements [20].

Nevertheless, systematic experimental and validated three-dimensional comparisons of heated rectangular, circular cylinder, equilateral triangle, and square obstacles in vertical air channels at identical imposed thermal and airflow conditions are still lacking, especially those that account for variations in characteristic length, frontal area, and blockage ratio while simultaneously assessing heat-transfer enhancement and pressure loss. Therefore, the current study provides a comparative analysis of symmetric pairs of these four heated obstacle geometries placed on opposite walls of the channel, based on both experimental and numerical validations. Similar exposed heat-transfer areas are preserved to control area-related bias, whereas the differences in characteristic length, frontal area, and blockage ratio that dictate flow separation, wake development, fluid mixing, and hydraulic resistance are accounted for directly. The three-dimensional model, validated against the experimental measurements, is used to assess the surface temperature, heat transfer coefficient (HTC), average *Nu*, and pressure drop, as well as the performance evaluation criterion (PEC), to find which thermo-hydraulic compromise within the operating range studied is optimal and gives indications for designers of compact cooling channels and heat exchangers.

2. MATERIALS AND METHODS

2.1 Experimental setup

A vertical rectangular air channel was designed to experimentally investigate the impact of different heated obstacle geometries on mixed-convection heat transfer and thermo-hydraulic performance. The experimental facility was a thermally insulated vertical duct with cross-sectional dimensions of 30 cm × 30 cm and a total height of 120 cm. The channel consisted of three sections, including the 30 cm inlet section, a 60 cm heated test section, and a 30 cm outlet. Such a configuration provided sufficient entry and exit lengths to allow for proper development of a stable flow through the test section (Figure 1).



Figure 1. Photograph of the experimental setup, (1) digital thermocouple thermometer, (2) Variac, (3) digital power meter, (4) digital anemometer, (5) exhaust fan, (6) digital differential pressure meter, and (7) heated test section

A perforated plate was introduced to enhance the uniformity of the incoming airflow at the channel entrance. Air was extracted via an exhaust fan located at the outlet section. Inlet air velocity was measured at the channel entrance using a digital anemometer.

The heated test section contained two interchangeable aluminum side plates mounted on the opposite sides of the duct. Each plate contained one heated obstacle, resulting in two identical obstacles arranged symmetrically in the test section. Four obstacle geometries were studied: rectangle, circular cylinder, equilateral triangle, and square. The obstacles were made of solid aluminum to provide high thermal conductivity and consistent thermal properties. The dimensions of the obstacles were also chosen to provide

almost identical exposed surface areas. In all the configurations investigated, the center of each obstacle was positioned at the midpoint of the test section, as shown in Figure 2. The inlet air velocity was measured at the channel entrance using a digital anemometer. generating an upward-through-flow scenario.

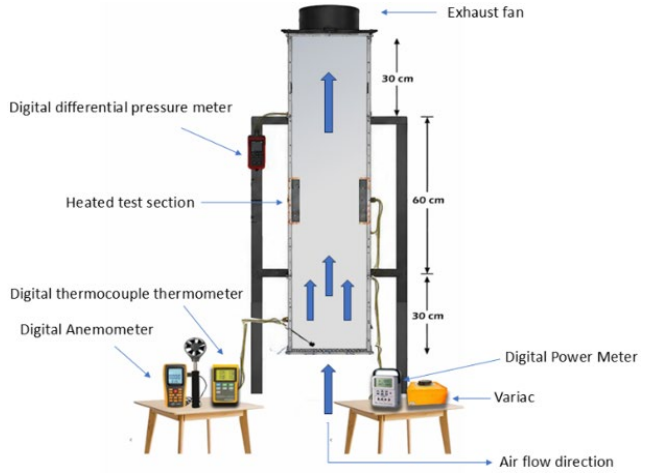


Figure 2. Schematic representation of the experimental setup showing the test airflow direction and measuring instruments

Photographs of the four investigated obstacle configurations installed symmetrically inside the test section are shown in Figure 3.

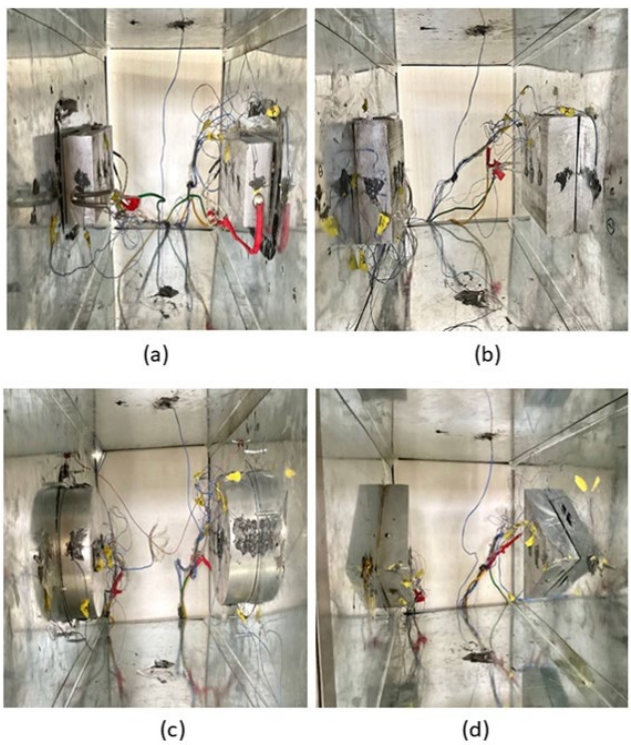


Figure 3. Photographs of the investigated obstacle configurations installed symmetrically inside the test section, (a) rectangle, (b) square, (c) circular cylinder, and (d) equilateral triangle obstacles

The obstacle dimensions and thermocouple locations are shown in Figure 4. Two resistive cartridge heaters were symmetrically embedded around the geometric center of each solid obstacle to provide internal heating for each obstacle. This was done to encourage a more uniform temperature throughout the surfaces, in which case there were minimal thermal gradients occurring. The current study considered two heating powers of 200 W and 300 W, which resulted in heat inputs equal to half the total power supplied by each obstacle, 100 W and 150 W for the corresponding heating powers.

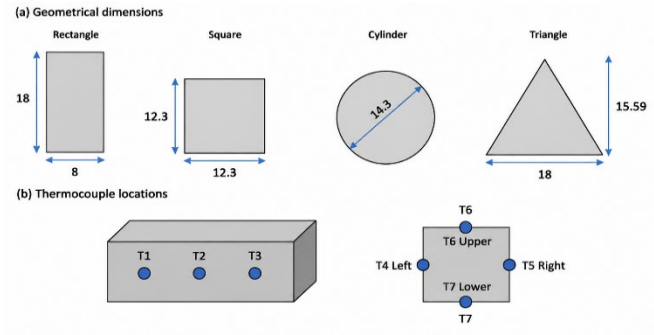


Figure 4. Dimensions of the investigated geometries and thermocouple locations

The dimensions of the obstacles were selected using a similar exposed heat-transfer area as the primary geometric criterion. The exposed area was defined as the front and lateral surfaces of each obstacle, while the wall-contacting base was excluded. As the nominal dimensions, the exposed area per obstacle had a range of 0.03403–0.03563 m², corresponding to a maximum difference of around 4.7%. Using a common protrusion thickness of 0.040 m for all configurations, identical mounting positions, inlet velocities, and heat inputs were maintained. Full equivalence of the characteristic length, frontal area, and blockage ratio was neither achievable nor desirable since these parameters are inherently determined by the obstacle geometry. Accordingly, the present comparison provides one with comparatively tuned obstacle configurations at an equal heated area in identical operating conditions rather than varying shape based on either a fixed characteristic length or aspect ratio.

For surface temperature measurements, type-K thermocouples were used. Each obstacle was monitored by seven thermocouples, three of which were placed on the front surface while one was installed on each of the exposed surfaces (upper, lower, left, and right faces) as illustrated in Figure 4. In addition, one of the thermocouples was placed at the inlet (T_{in}) and another at the outlet (T_{out}) to measure the air temperatures at the inlet and outlet of the channel. For all these temperature measurements of the system, a multi-channel digital thermocouple thermometer was used after the system reached steady-state conditions. The power to the cartridge heaters was controlled using a variable AC voltage regulator (Variac) and continuously monitored via a digital power meter to ensure constant heat input during the experiments.

The hydraulic performance of the tested configurations was assessed by measuring the pressure drop across the test section using a digital differential pressure meter connected through flexible tubes to pairs of pressure taps inserted at the inlet and outlet sections.

2.2 Experimental procedure

A symmetric pair of identical obstacles was mounted at fixed horizontal positions on the opposite walls of the test section before each run. The cartridge heaters were connected

to an electrical power source through a variac, and the inlet air velocity was controlled. Once steady state was reached, the obstacle surface temperatures, inlet and outlet air temperatures, inlet air velocity, and pressure drop across the test section were recorded. Ambient temperatures were recorded via Type-K thermocouples and a 12-channel temperature recorder (Lutron BTM-4208SD), and the supplied power was measured using a Lutron DW-6091 power analyzer. Thermocouples and the temperature recorder had accuracies of ±0.5 ℃ and (±(0.4% of the reading + 0.5 ℃)), respectively. After each trial, the heaters and fan were turned off, and the apparatus was allowed to return to near-ambient temperature before the next operating condition was initiated. Once all ten operating conditions for one geometry were conducted, the obstacle pair was replaced, keeping them in the same installations and experimental procedure. Experimentally determined instrument accuracies specified by the manufacturer were used to quantify experimental reliability, and one considered representative rectangular-obstacle case was repeated. The two runs resulted in average surface temperatures of 458.259 and 460.000 K, HTC of 18.800 and 18.586 $W \cdot m^{-2} \cdot K^{-1}$, and mean *Nu* of 126.745 and 125.301, respectively. The percentage differences for the mean surface temperature and the HTC and average *Nu*, defined relative to the mean of their respective duplicate values, were 0.38% and approximately 1.15% for both HTC and average *Nu*, showing good repeatability at this operating condition. The associated uncertainties were estimated to be ±1.34 ℃ at a typical surface temperature of 460 K for the combined temperature measurement, while the power measurement uncertainties were ±8 W at 200 W and ±9.5 W at 300 W, respectively, since HTC and *Nu* values are dependent on those supplied powers along with the measured temperature difference, heat-transfer area, and characteristic length.

3. NUMERICAL METHODOLOGY

3.1 Computational domain and numerical model

A three-dimensional numerical model was built in COMSOL Multiphysics 6.3 to replicate the vertical air channel experimental configuration and analyze how different internal geometries influence the mixed-convection heat-transfer characteristics. The computational domain is a square channel with a full size of 30 × 30 × 120 cm, comprising a 30 cm inlet section, a 60 cm test section, and a 30 cm outlet section. Under suction conditions, air was introduced into the channel from its lower side and passed through the inner space before exiting the upper boundary linearly, as per the experimental arrangement. Two identical aluminum obstacles were symmetrically positioned on the opposite walls at the center of the testing section. Four different geometries of obstacles were studied: a rectangle, a circular cylinder, an equilateral triangle, and a square. The orientation of the equilateral triangle was with its apex facing into the flow. The same thermal and hydrodynamic boundary conditions were applied to all geometries in order to provide a fair comparison.

The air and aluminum were assigned to the fluid and solid domains, respectively, with their thermophysical properties taken from the COMSOL material library. Heat transfer in solids and fluids and turbulent flow: shear-stress transport (SST) interfaces were used to solve the coupled heat-transfer and fluid-flow problem. The SST model was chosen to simulate turbulence, as it can ability to predict near-wall flows and weakly separated regions while remaining robust in the free stream region.

The Boussinesq approximation was used to account for the buoyancy effects driven by temperature gradients, and gravitational acceleration was included in the momentum equations. This was the reference temperature used in the simulations:

$$T_{\mathrm{ref}} = 293.15\ \mathrm{K}$$

In the Boussinesq formulation, density differences were ignored in all but the buoyancy term to reduce computational cost while still providing accurate estimates of mixed-convection predictions.

3.2 Boundary conditions and numerical assumptions

At the channel inlet, a uniform velocity profile was specified. Five inlet velocities were investigated:

$$U_{\mathrm{in}} = 2,\ 3,\ 4,\ 5,\ 6\ \mathrm{m\,s^{-1}}$$

To ensure consistency between the experiments and numerical analyses, the inlet temperature for each numerical case was set to match the experimental measurements that ranged from 299 to 306.6 K. At the upper extremity of the channel, a pressure-outlet boundary condition was implemented, while an outflow thermal condition was applied, which allowed heat to exit through convection from the computational domain. All solid surfaces were assigned no-slip boundary conditions, and the external walls of the channel were assumed to be adiabatic. In addition, thermal continuity was enforced at all fluid–solid interfaces. COMSOL has several formulations for heat, and one is the heat rate that was used to model heating at 200 W and 300 W. Heat was uniformly generated in the aluminum domains to represent thermal energy input from within the cartridge heaters.

3.3 Governing equations and shear-stress transport k−ω model

The numerical model was formulated using COMSOL Multiphysics 6.3 for steady-state three-dimensional turbulent flow of incompressible air using the Boussinesq approximation. Fluid flow and heat transfer were modeled; thermal radiation and external heat losses were ignored, and perfect thermal contact was assumed at all the fluid–solid interfaces.

The near-wall region was also treated using the automatic wall-treatment option of the SST model, which varies between wall functions and a low *Re* formulation according to the local mesh resolution. The governing equations were solved using a stationary segregated scheme with pseudo-time-stepping stabilization. Before solving the stationary solution, a wall-distance initialization step was performed, and convergence was evaluated using the solution-or-residual criterion with a relative tolerance of 10^{-3} and a maximum of 400 iterations.

The mass conservation, momentum conservation, and energy conservation equations were used to model the thermo-fluid behavior in the vertical channel. The governing equations were numerically solved using the finite-element method in COMSOL Multiphysics 6.3. The present investigation

considered turbulent mixed convection. Therefore, the Reynolds-averaged Navier-Stokes (RANS) equations were coupled with the SST turbulence model. Meanwhile, the Boussinesq approximation was used to include buoyancy effects. The governing equations are expressed as follows:

$$\nabla \cdot u = 0 \tag{1}$$

$$\rho(\mathrm{u} \cdot \nabla \mathrm{u}) = -\nabla \mathrm{p} + \nabla \cdot [\mu(\nabla \mathrm{u} + (\nabla \mathrm{u})^{\mathrm{T}})] + \rho \mathrm{g} + \mathrm{F} \tag{2}$$

$$\rho = \rho_{\mathrm{ref}}[1 - \beta_T(T - T_{\mathrm{ref}})] \tag{3}$$

$$\rho C_p(u \cdot \nabla T) = \nabla \cdot (k \nabla T) + Q_v \tag{4}$$

$$\rho(u \cdot \nabla k) = \nabla \cdot [(\mu + \sigma_k \mu_t)\nabla k] + P_k - \beta^* \rho k \omega \tag{5}$$

$$\rho(u \cdot \nabla \omega) = \nabla \cdot [(\mu + \sigma_\omega \mu_t)\nabla \omega] + \alpha \frac{\omega}{k} P_k - \beta \rho \omega^2 + D_\omega \tag{6}$$

To evaluate the thermal, hydrodynamic, and overall thermo-hydraulic performance of the investigated configurations, *Re*, *Ri*, Grashof number (*Gr*), convective HTC, bulk fluid temperature, average *Nu*, pressure drop, and PEC were calculated using the following expressions:

$$Re = \frac{\rho U D_h}{\mu} \tag{7}$$

$$Ri = \frac{Gr}{Re^2} \tag{8}$$

$$Gr = \frac{g \beta_T (T_s - T_b) D_h^3}{\nu^2} \tag{9}$$

$$h = \frac{Q}{A(T_s - T_b)} \tag{10}$$

$$T_b = \frac{T_{\mathrm{in}} + T_{\mathrm{out}}}{2} \tag{11}$$

$$Nu = \frac{hL_c}{k} \tag{12}$$

$$\Delta P = P_{in} - P_{out} \tag{13}$$

$$PEC = \frac{Nu/Nu_{\mathrm{sq}}}{(\Delta P/\Delta P_{\mathrm{sq}})^{1/3}} \tag{14}$$

Characteristic lengths utilized to calculate the average *Nu* are summarized in Table 1.

Table 1. Characteristic lengths of the investigated obstacle geometries

Shape	Rectangle	Circular Cylinder	Equilateral Triangle	Square
$L_c(cm)$	18	14.3	15.588	12.3

The characteristic length corresponding to each obstacle geometry was selected as the principal dimension parallel to the incoming airflow. This approach is consistent with previous studies on mixed convection around bluff bodies and allows the heat-transfer performance of different geometries to be evaluated using the conventional definition of the average *Nu*. It should be noted that, in addition to the average *Nu*, the HTC and PEC were also employed to provide a more comprehensive comparison among the investigated geometries.

3.4 Mesh independence study

A mesh-independence study was also carried out to ensure that the numerical predictions were not sensitive to grid resolution. The average *Nu* was used as a monitoring parameter to evaluate three physics-controlled mesh levels—coarse, normal, and fine—under one representative operating condition. Included active mesh constituents are heat transfer in solids and fluids, turbulent flow models, SST, and nonisothermal flow. The mesh consisted of an unstructured tetrahedral core and automatically generated boundary-layer elements adjacent to all no-slip surfaces, including the heated obstacles, with refinement along flaws at the edges and corners of obstacles. Relative deviation with respect to the fine mesh was calculated—as summarized in Table 2.

Table 2. Grid-independence study for the representative operating condition

Mesh Type	Number of Elements	Average Nusselt Number (*Nu*)	Relative Error (%)	Mesh Type
Coarse	484,778	196.4026	5.54	Coarse
Normal	1,090,458	202.6795	2.52	Normal
Fine	3,414,373	207.9225	0.00	Fine

The normal mesh estimated an average *Nu* that differed by only 2.52% from the fine-mesh result. However, the fine mesh containing 3,414,373 elements was retained for all simulations to maximize numerical accuracy and ensure a consistent meshing approach for the four obstacle geometries. A mesh consisted of an unstructured tetrahedral core and automatically generated boundary-layer elements corresponding to all no-slip surfaces, including the heated obstacles, with local refinement along the edges and angles of the obstacles, as shown in Figure 5.

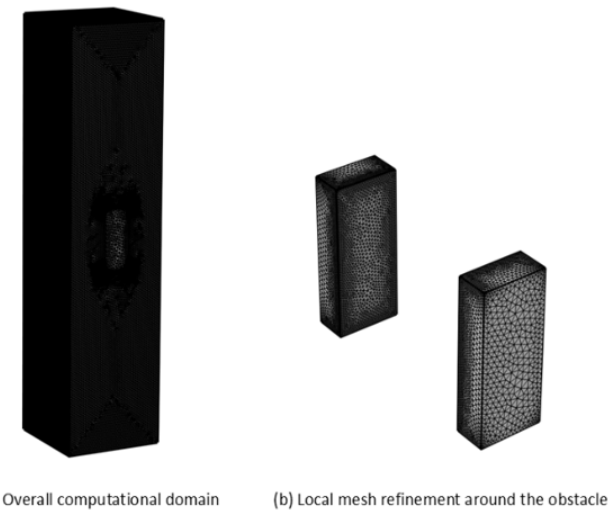


Figure 5. Computational mesh used in the numerical simulations, (a) overall computational domain and (b) local mesh refinement around the heated obstacle

4. RESULTS AND DISCUSSION

4.1 Validation of the numerical model

In order to evaluate the validity of the developed numerical model, the predicted average *Nu* values were compared with their experimental counterparts obtained under exactly the same operating conditions.

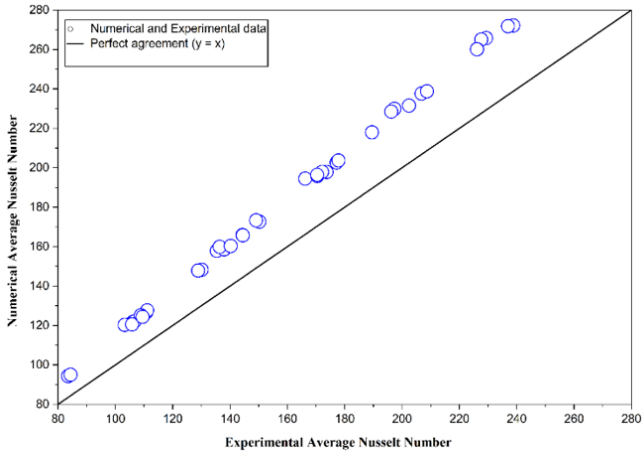


Figure 6. A comparison between the averaged Nusselt numbers (*Nu*) is shown comparing the experimental and numerically obtained values for all geometries and operating conditions over the considered Reynolds number (*Re*) range

As illustrated in Figure 6, the numerical predictions follow the experimental trends for every analyzed obstacle geometry, with most data points located close to the line of perfect agreement. The absolute relative deviation between the numerical and experimental average *Nu* was calculated as follows $\delta_{Nu}(\%) = \left|\frac{\overline{Nu}_{num} - \overline{Nu}_{exp}}{\overline{Nu}_{num}}\right| \times 100.$

The numerical model systematically overestimates the average *Nu*, with deviations ranging from 10% to 15% error levels. These deviations were attributed to a combination of experimental and numerical uncertainties. Due to unavoidable heat losses through the insulation, supporting plates, and heater connections, the effective thermal conditions of the experiments may differ from the prescribed heat input in reality. Additionally to thermocouple accuracy and surface contact, potential errors may result from small variations in inlet airflow and duct dimensions, including obstacle geometry, spacing, and alignment. The respective numerical model in turn assumes perfect geometry, a symmetric configuration of obstacles, uniform conditions at the inlet, a constant rate of heat input, smooth boundary surfaces, ideal thermal contact, and adiabatic external walls. The Boussinesq approximation and SST turbulence model also introduced some simplifications regarding actual thermo-fluid behavior. However, the prevailing trends and small deviations indicated that the validated model represented most of the dominant thermo-fluid features reasonably well, such that informed comparisons could be made among the geometries investigated over the range of operating conditions considered.

4.2 Temperature distribution and flow structure

The temperature field around the four analyzed obstacle geometries is depicted in Figure 7. In all cases, the highest temperature occurred at the heated obstacle surfaces, while air temperature decreases away from these surfaces. A thermal boundary layer formed adjacent to the heated surfaces, while the airflow transported heat downstream.

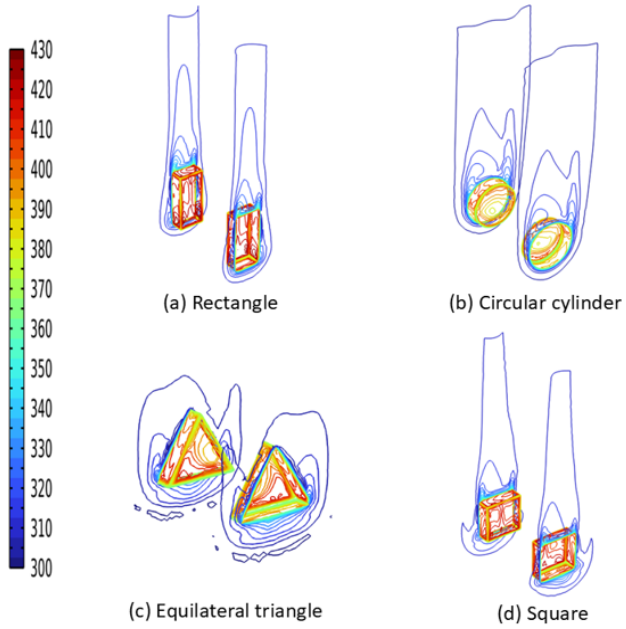


Figure 7. Temperature contours for the investigated geometries, (a) rectangle, (b) circular cylinder, (c) equilateral triangle, and (d) square at a heating power of 300 W and an air velocity of 6 m/s

Significant differences in the thermal field were detected between different shapes of the obstacle out of all investigated geometries. The rectangular obstacle generated a longer heated region in the downstream direction, showing stronger interaction of the heated surface with the main airflow. Such increased interaction gave rise to thermal mixing, which in turn was responsible for the larger *Nu* obtained for the rectangular geometry. On the other hand, a circular cylinder provided a more uniform temperature distribution over its curved surface, while localized hot-spot formation occurred at sharp corners of triangular obstacles. Due to the stronger flow stagnation at leading edges, the square geometry created larger high-temperature regions near its flat surfaces. As a result, the increase in stagnation regions decreases the performance of convective heat transfer compared with the other geometries. In summary, the contour plots show that the geometry of an obstacle has an important effect on how the thermal boundary layer grows and how temperature is distributed inside the vertical channel. The differences observed in the thermal field are closely related to the effects of obstacle geometry on the development of the thermal boundary layer. The rectangular obstacle led to greater interaction with the main airflow, enhancing heat transfer between the surface and adjacent fluid. As a result, the thermal boundary layer was reduced, thus augmenting convection heat transfer. On the other hand, the square obstacle produced large stagnation zones in its near leading edges, which limited local fluid motion and reduced heat transfer from the heated faces.

4.3 Flow structure analysis

Velocity contours show that the impact of the internal obstacles significantly changes the flow structure inside the vertical channel, as shown in Figure 8. The effective flow area

was decreased, and hence regions of accelerated flow were observed around the obstacle edges, while low-velocity wake regions immediately downstream of the heated bodies were formed by flow separation.

The rectangle induced the strongest flow acceleration and mixing due to its elongated geometry and sharp leading edges. The rectangular geometry increased the flow acceleration and resulted in increased velocity gradients and hence momentum transport near the heated surfaces. But a greater pressure-drop penalty with respect to the geometries investigated in this work also results from the stronger wake region, which forms downstream.

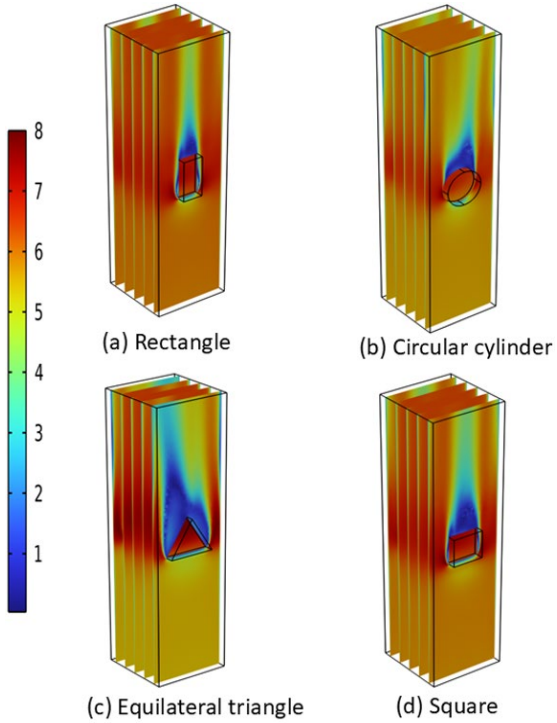


Figure 8. Velocity contours of the investigated geometries: (a) rectangle, (b) circular cylinder, (c) equilateral triangle, and (d) square at a heating power of 300 W and an air velocity of 6 m/s

On the other hand, with a circular cylinder, this will smooth out the flow path, and the flow separation was weaker. The triangular configuration, with its slanted faces and sharp turns, had the most complex flow structures, followed by the square geometry that displayed intermediate behavior between those of the triangle and circular cylinder.

The different obstacle geometries imposed different blockage effects on the flow field. Geometries with sharp edges accelerate the surrounding flow and enhance momentum exchange, while smoother shapes reduce fluid separation and yield velocity distributions more similar to one another. This can lead to differences in flow acceleration and wake formation, which have a direct impact on thermal boundary-layer thickness and thus impact the heat-transfer performance.

4.4 Streamline analysis

The temperature-colored streamlines in Figure 9 demonstrate how the heated air is entrained within the upward bulk flow, while the obstacle geometry governs deflection, separation, and wake development of any ensuing thermal plume. The smoother flow around the sides of a circular cylinder resulted from its curved surface, which limited the development of extended corner-stagnation regions and led to the maximum HTC and generally lower surface temperature.

The blunt leading edges of rectangular and square obstacles produced strong upstream stagnation and sharp edge separation at their corners. The *Nu* of the rectangle was larger, mainly due to its larger characteristic length, but the smaller frontal projection limited hydraulic resistance. Although the upstream apex of the triangular obstacle separated incoming flow into two shear layers and created strong downstream wake interaction, its larger blockage increased pressure-loss penalties. These results showed that greater recirculation or mixing was not always ideal for overall performance unless also considering hydraulic loss.

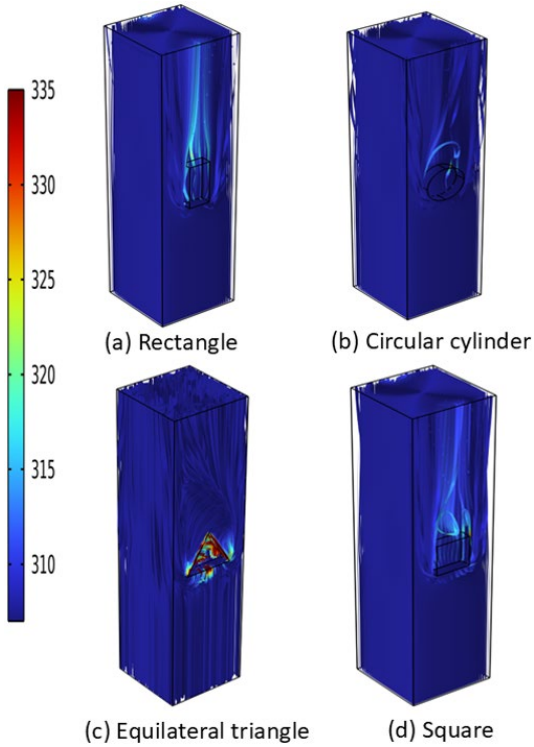
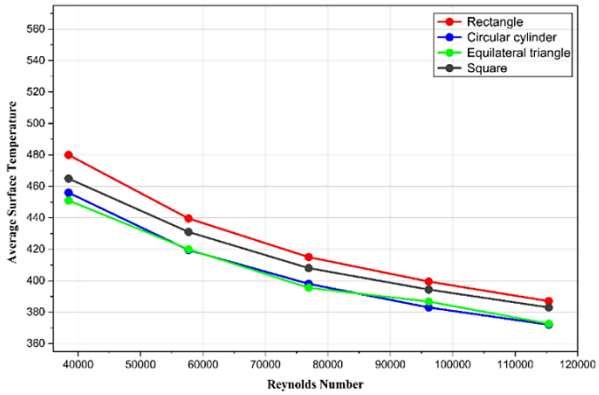


Figure 9. Temperature-colored streamlines for the investigated geometries, (a) rectangle, (b) circular cylinder, (c) equilateral triangle, and (d) square at a heating power of 300 W and an air velocity of 6 m/s

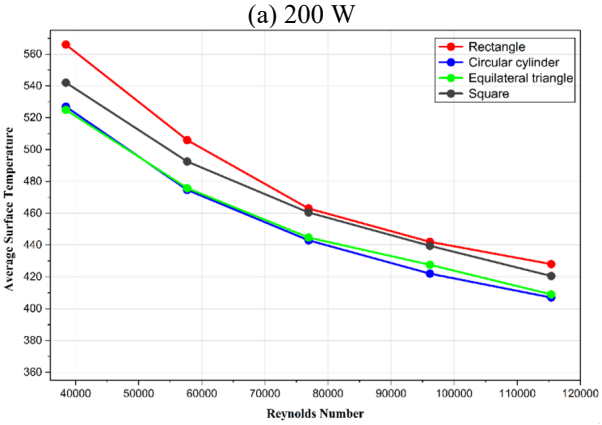
4.5 Effect of Reynolds number on average surface temperature

As shown in Figure 10, the average surface temperature for all geometries studied decreased as *Re* increased due to an increase in forced convection and a decrease in thermal boundary-layer thickness. Higher air velocity improved heat extraction from the heated surfaces, leading to lower surface temperatures.

In this regard, the rectangular geometry showed the highest maximum surface temperatures for both heating powers. On the other hand, much lower surface temperatures of the placed circular cylinders and equilateral triangles resulted from their streamlined shapes, which helped enhance flow mixing and subsequently augment heat transfer. Intermediate behavior was shown by the square geometry. An increase in heating power from 200 to 300 W caused the temperature curves to be higher for all geometries, but the characteristic of change is preserved.

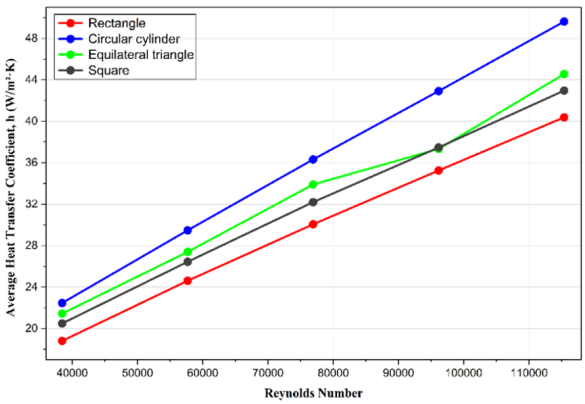


(a) 200 W

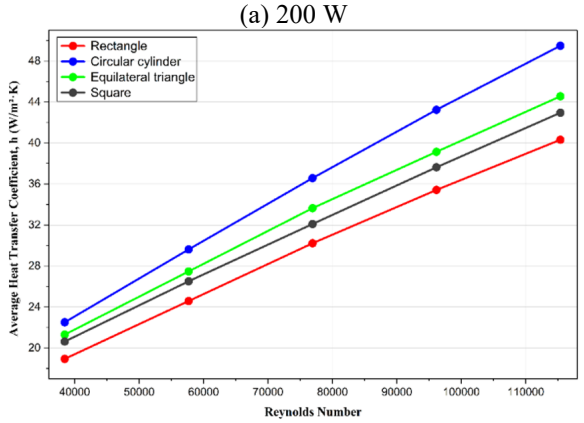


(b) 300 W

Figure 10. Variation of the average surface temperature with Reynolds number (*Re*) for the investigated geometries at (a) 200 W and (b) 300 W



(a) 200 W



(b) 300 W

Figure 11. Variation of the average heat transfer coefficient (HTC) with Reynolds number (*Re*) for the investigated geometries at (a) 200 W and (b) 300 W

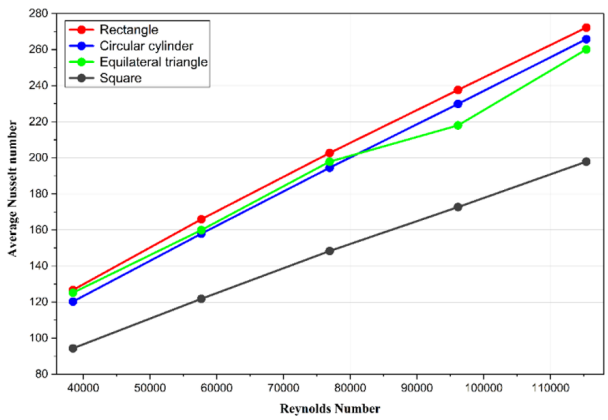
4.6 Effect of Reynolds number on heat transfer coefficient

As shown in Figure 11, the average HTC increased with increasing *Re* for all geometries due to the forced convection improvement and reduction in thermal resistance. Fluid mixing was intensified in the region, which led to heat transfer from heated surfaces at higher *Re*.

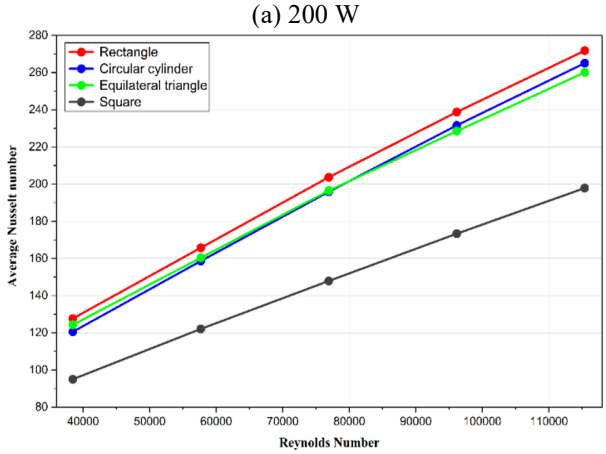
The most important finding is that, for all *Re* ranges, the HTC of the circular cylinder is maximum, and what you find out is that the rectangular geometry transfers the minimum values. The behavior of the equilateral triangle and square geometries was intermediate. The difference was mainly due to the influence of obstacle shape on flow structure and the development of thermal boundary layers.

4.7 Effect of Reynolds number on average Nusselt number

As shown in Figure 12, the average *Nu* increases systematically with *Re* for all examined geometries. An increase in inlet velocity intensified the inertial effects contributing to enhanced velocity and thermal gradients within the boundary layers near the heated surfaces while also favoring entrainment of cooler core air into the separated shear layers. Therefore, the thermal boundary layer became thinner and redeveloped behind the blocks, which led to an increase in HTC as well as average *Nu*. The circular cylinder had the highest heat-exchange coefficient due to its smooth, near-surface flow over the curved surface without stagnant corner regions. In contrast, the rectangular obstacle produced the highest average *Nu*, and the square generated the lowest ones.



(a) 200 W



(b) 300 W

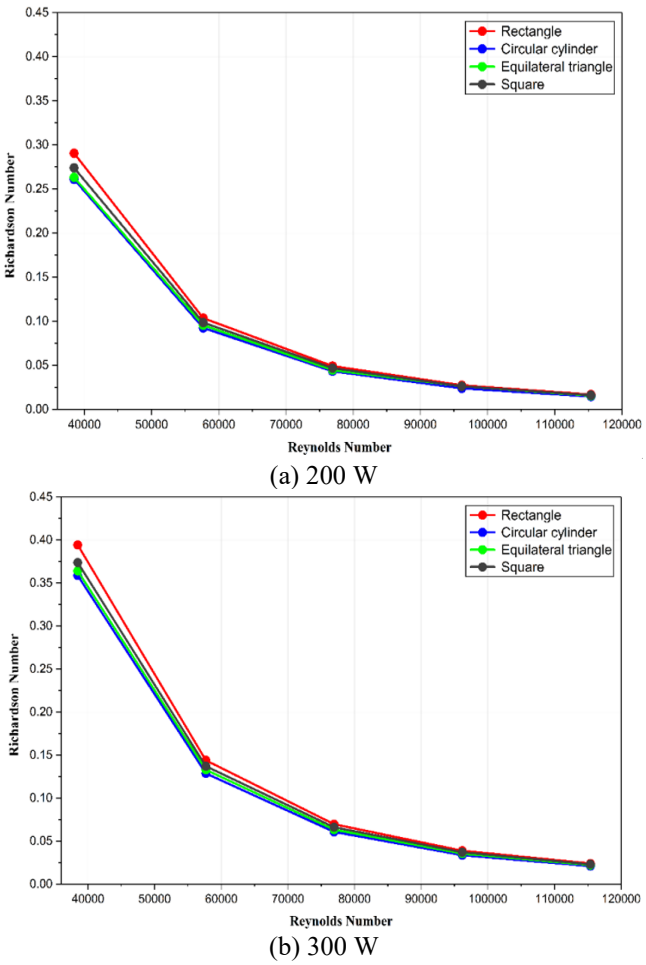
Figure 12. Variation of the average Nusselt number (*Nu*) with Reynolds number (*Re*) for the investigated geometries at (a) 200 W and (b) 300 W

Thus, the larger characteristic length for the rectangle (0.180 m) was directly responsible for its larger *Nu* even when its HTC was lower than that of the circular cylinder. Moreover, its sharp leading corners enhanced flow separation and shear-layer mixing, while a smaller transverse width reduced frontal blockage and produced a narrower wake downstream of the obstacle compared with those of wider square and triangular obstacles. This combination provided good fluid mixing without incurring an excessive pressure-drop penalty. Thus, this rectangular geometry achieved the highest PEC over the studied operating period.

4.8 Mixed-convection analysis using Richardson number

As shown in Figure 13, *Ri* for all geometries investigated at different *Re* decreased strongly with increasing *Re*, confirming that buoyancy effects are progressively suppressed as inertial forces became dominant. Higher airflow velocity enhanced forced convection and promoted flow behavior to a forced-convection regime. At low *Re*, the flow remained in the mixed convection regime, while at higher *Re*, forced convection became the dominant heat-transfer mechanism. Moreover, a continuous increase in the heating power causes a bigger difference in local density, which leads to a more positive *Ri* from 200 W to 300 W.

This demonstrates that both *Re* and heating power were key factors influencing the relative contributions of natural convection and forced convection within the vertical channel.



(a) 200 W

(b) 300 W

Figure 13. Variation of Richardson number (*Ri*) with Reynolds number (*Re*) for the investigated geometries at (a) 200 W and (b) 300 W

4.9 Thermo-hydraulic performance evaluation

The thermo-hydraulic performance of the examined geometries was evaluated using pressure drop and the performance assessment criterion (PEC). The pressure drop increased with *Re* for all configurations because higher airflow velocity increased inertial and form-drag losses. The square configuration was adopted as the common reference, and so its PEC could be set to unity.

The rectangular obstacle gave the highest PEC value of approximately 1.40 at the maximum *Re* investigated with both (Q = 200) W and (Q = 300) W powers. Although the circular cylinder gives the highest HTC, the rectangle manufactured high increments in HTC to hydraulic losses ratios in the present investigation conditions.

While the exposed areas were similar, their geometries had different characteristic lengths and blockage ratios. A direct reason for its higher *Nu* is the bigger characteristic length in the width of the rectangle compared to its area-weighted average. The blockage ratios of the symmetric obstacle pairs were 7.11%, 10.93%, and 12.71%, and the rectangle, square, circular cylinder, and triangle obstacles were tested as a pair with a filling ratio, respectively. Thus, the reduced hydraulic penalty conferred by the lower blockage of the rectangle and the higher blockage of the triangle elevated resistance to flow. This PEC ranking was a consequence of the production exerted by characteristic length, projected frontal area, laws of separation and wake development, and blockage. Higher pressure drops also raise the fan power needed to maintain a prescribed airflow rate from an engineering-design standpoint. Thus, the heat-transfer enhancement provided by the rectangular obstacle, with a PEC of approximately 1.40, compensated for its additional hydraulic penalty in comparison to the square reference. When both cooling performance and fan-power demand are included in the analysis, the rectangle was therefore the preferred design among those investigated. Circular cylinders may still be the best choice when maximum HTC is needed and a higher hydraulic penalty is acceptable, while the larger blockage and pressure loss of a triangular obstacle present challenges for fan-power-limited systems. The square layout is the baseline condition and not an effective efficiency standard. Because PEC is a combined thermo-hydraulic index, it cannot be interpreted as a direct percentage increase in heat transfer or decrease in energy consumption. These design implications are limited to the investigated airflow conditions, heating powers, *Re* range, and obstacle configurations.

5. CONCLUSION

In the current detailed numerical and experimental research, heat transfer by mixed convection in a vertical air channel with four different internal wall geometries is studied experimentally and numerically; each geometry comprises an arrangement of rectangular, circular cylindrical, equilateral triangle, or square. In view of the results obtained, the following conclusions can be drawn:

1. The numerical model developed in COMSOL Multiphysics provided predictions that agreed with the experimental measurements with deviations of 10 % to 15%, confirming this numerical methodology as a reliable tool for predicting mixed-convection heat transfer inside the channel.
2. For all the geometries studied in this investigation,

increasing Re improved the convective heat-transfer process with larger average HTC and *Nu* and smaller average surface temperatures. With increasing *Re*, the average surface temperature decreased continuously because of the enhancement of forced convection and decreasing thermal boundary-layer thickness.

3. The circular cylinder had the highest average HTC in this study because its curvature reduced stagnant-flow regions while facilitating a more uniform flow distribution.

4. The rectangular geometry showed the highest average *Nu* over the investigated *Re* range. At the highest *Re*, the *Nu* reached a maximum value of approximately 272 as the maximum average *Nu*, showing the superior heat transfer at this condition.

5. The *Ri* decreased considerably with increasing *Re*, indicating a mixed convection regime at lower airflow velocities, with forced convection prevailing at higher streamwise velocities within the investigated operating range.

6. Contour and streamline analyses indicated that the obstacle geometry considerably affected both the flow structure formed in the channel as well as thermal boundary layer development and wake formation inside the vertical channel.

7. The pressure drop increased with increasing *Re* for all geometries examined. In addition, the square configuration was used as the reference for the PEC calculation and designated with a unit PEC value. Note that this selection was applied for normalization and did not imply that the square obstacle always generated the lowest pressure drop.

8. Among the four configurations investigated, the rectangular geometry achieved the highest PEC (1.40) according to thermo-hydraulic analysis. This ranking is only valid for the state of air as a working fluid, total heating powers of 200 and 300 W, a *Re* range between 38,462 and 115,385, and the specified channel dimensions, obstacle sizes, and obstacle arrangement. Thus, the rectangular obstacle should be regarded as the best-performing configuration only in the examined range, but not as a universally optimal design. Changes in the working fluids, heating power, Re, blockage ratios or obstacle dimensions, and spacings may alter the balance between heat-transfer enhancement and pressure loss. Further studies should investigate broader operating and geometrical ranges in order to evaluate the general validity of the current ranking.

9. The rectangular geometry had a PEC of nearly 1.40 and offered the ideal hydro-thermal trade-off within the tested 0.30 × 0.30 m vertical air channel with two symmetrically positioned obstacles. Nonetheless, as the obstacles had similar exposed areas but different characteristic lengths and blockage ratios, this ranking pertains specifically to the investigated configurations and operating range, which does not solely concern the shape of the obstacle and could change under different geometric or operating conditions.

REFERENCES

[1] Trad, N., Henniche, R., Korichi, A. (2026). Enhanced heat transfer in a vertical heated channel by incorporation of inclined plates. Journal of Heat and Mass Transfer Research, 13(1): 1-17. https://doi.org/10.22075/jhmtr.2025.37223.1700

[2] Ozdemir, S., Kilic, M., Çalışır, T., Başkaya, Ş. (2022). Numerical investigation of enhancing mixed convection heat transfer by using semi-cylindrical obstacles in a vertical channel. Isi Bilimi ve Teknigi Dergisi-Journal of Thermal Science and Technology, 42(1): 1-16. https://doi.org/10.47480/isibted.1106571

[3] Liu, Z.H., Wang, J., Ni, M.J., Zhang, N.M. (2024). Unsteady mixed convection flows in a rectangular duct and dynamical behaviors of flow channel insert. International Journal of Energy Research, 2024(1): 5510119. https://doi.org/10.1155/2024/5510119

[4] Howland, C.J., Yerragolam, G.S., Verzicco, R., Lohse, D. (2024). Turbulent mixed convection in vertical and horizontal channels. Journal of Fluid Mechanics, 998: A48. https://doi.org/10.1017/jfm.2024.598

[5] Chong, D., Liu, J., Yan, J., Zhou, Z. (2007). Experimental investigation of mixed convection in a rectangular duct with a heated plate in the middle of cross section. Heat and Mass Transfer, 43(12): 1283-1291. https://doi.org/10.1007/s00231-006-0214-7

[6] Pasa, D., Pulagam, M.K.R., Rout, S.K., et al. (2026). Influence of fin geometry on heat transfer and friction in plate fin heat exchangers: A CFD approach. Journal of Engineering and Applied Science, 73(1): 314. https://doi.org/10.1186/s44147-026-01155-8

[7] Boukhari, A., Khechekhouche, A., Keddouda, A., Jahangiri, M., de Oliveira Siqueira, A.M., Campos, J.C.C. (2025). Numerical investigation of mixed convection heat transfer in three-dimensional ventilated enclosure containing a T-shaped heat fin: Effects of dimensionless numbers. Journal of Engineering, 2025(1): 2330154. https://doi.org/10.1155/je/2330154

[8] Ikumapayi, O.M., Kaid, N., Larguech, S., et al. (2025). Optimizing heat transfer in laminar channel flow using inclined inverted L-shaped obstacles. Thermal Science, 29(4B): 3219. https://doi.org/10.2298/tsci2504219i

[9] Admi, Y., Moussaoui, M.A., Mezrhab, A. (2022). Numerical investigation of convective heat transfer and fluid flow past a three-square cylinders controlled by a partition in channel. International Journal of Renewable Energy Development, 11(3): 766-781. https://doi.org/10.14710/ijred.2022.43790

[10] Kumar, B.V., Kanna, P.R., Manikandan, G., et al. (2023). Investigation of thermo-hydraulic performances of artificial ribs mounted in a rectangular duct. Energies, 16(11): 4404. https://doi.org/10.3390/en16114404

[11] Al-Mayahi, H.A., Hamza, Z.A., Hacham, W.S., Yaseen, S.J. (2026). Numerical analysis of mixed convection in vented triangular cavity with bottom-mounted adiabatic fin. International Journal of Heat and Technology, 44(1): 45-58. https://doi.org/10.18280/ijht.440105

[12] Mirshafiee, S.M., Amiri, E.O. (2021). Numerical investigation of heat transfer in a rectangular channel with square baffles and a triangular obstacle. International Journal of Heat and Technology, 39(2): 597-603. https://doi.org/10.18280/ijht.390230

[13] Nguyen, Q.D., Ji, S., Lei, C. (2024). A numerical study of natural convection through a vertical heated channel with a confined circular cylinder. Physics of Fluids, 36(3): 033628. https://doi.org/10.1063/5.0201307

[14] Lee, J.S., Ha, M.Y., Min, J.K. (2021). Numerical study on the mixed convection around inclined-pin fins on a heated plate in vertical channels with various bypass ratios. Case Studies in Thermal Engineering, 27: 101310. https://doi.org/10.1016/j.csite.2021.101310

[15] Talbi, H., Ghoulam, O., Mir, A., Amghar, K., Charef, A.

(2026). CFD study of obstacle orientation and arrangement effects on thermo-hydraulic performance in turbulent channel flow. Next Chemical Engineering, 3: 100068. https://doi.org/10.1016/j.nxcen.2026.100068

[16] Ji, S., Nguyen, Q.D., Gan, Y., Lei, C. (2025). A numerical study of blockage and inclination effects on natural convection in a uniformly heated air flow channel. International Journal of Thermal Sciences, 212: 109783. https://doi.org/10.1016/j.ijthermalsci.2025.109783

[17] Alsabery, A.I., Salih, S.M., Ismael, M.A., Hussein, A.K., Hashim, I., Jalil, J.M. (2024). Enhancement of cooling process of hot blocks mounted inside a horizontal channel using flexible baffles—Alternative arrangement. International Journal of Thermofluids, 23: 100805. https://doi.org/10.1016/j.ijft.2024.100805

[18] Zhang, G., Sundén, B., Xie, G. (2021). Combined experimental and numerical investigations on heat transfer augmentation in truncated ribbed channels designed by adopting fractal theory. International Communications in Heat and Mass Transfer, 121: 105080. https://doi.org/10.1016/j.icheatmasstransfer.2020.105080

[19] Adhikari, R.C., Wood, D.H., Pahlevani, M. (2020). An experimental and numerical study of forced convection heat transfer from rectangular fins at low Reynolds numbers. International Journal of Heat and Mass Transfer, 163: 120418. https://doi.org/10.1016/j.ijheatmasstransfer.2020.120418

[20] Henniche, R., Korichi, A. (2025). Mixed and forced convection heat transfer in baffled channels: A brief review. Journal of Heat and Mass Transfer Research, 12(1): 15-28. https://doi.org/10.22075/JHMTR.2024.34280.1565

NOMENCLATURE

L_c	characteristic length, m
h	heat transfer coefficient (HTC), W m^{-2} K^{-1}
Re	Reynolds number, dimensionless
Ri	Richardson number, dimensionless
Gr	Grashof number, dimensionless
PEC	performance evaluation criterion, dimensionless
Nu	Nusselt number
Q	supplied heat input, W
SST	shear stress transport

Greek symbols

β_T	thermal expansion coefficient, K^{-1}
β^*	SST turbulence-model coefficient, dimensionless
β	SST turbulence-model coefficient, dimensionless
ΔP	pressure drop, Pa
μ	dynamic, Pa·s
ν	kinematic viscosities, m^2·s^{-1}
ρ	air density, kg m^{-3}
ω	specific dissipation rate, s^{-1}